Projection and detection of climate change impact on fatigue damage of offshore floating structures operating in three offshore oil fields of the North Sea

Tao Zou[1] [ORCID] · Miroslaw Lech Kaminski[2]

Abstract

Fatigue damage of offshore floating structures is a long-term cumulative process, which is mainly attributed to ocean waves. The natural variability and human-induced climate change may affect the wave climate and consequently result in the change of fatigue damage. This paper aims to investigate the effect of climate change on the fatigue damage of offshore floating structures operating in three offshore oil fields of the North Sea (Alma/Galia, Pierce, and Rosebank oil fields, located in 56.2° N/2.8° E, 58° N/1.45° E, and 61° N/4° W latitude/longitude). Then it can detect whether human-induced climate change has a considerable impact on fatigue damage. Therefore, firstly the natural variability of wave height and fatigue damage was investigated through 30-year control simulations by coupling wave models to climate models, ignoring the effect of human activities. After that the sea states and annual fatigue damages were projected in three decadal periods (2011–2020, 2051–2060, and 2091–2100) based on widely recognized climate scenarios including the greenhouse gas emission trajectories. The effect of human-induced climate change has been detected, and it has been found that the higher the emission, the less the fatigue damage in considered floating structures in the North Sea. In addition, although wave height is the dominant wave characteristic in fatigue calculations, the change of other wave characteristics should also be considered to improve the quality of fatigue designs.

Keywords Climate models · Wave models · Climate change · Fatigue damage · Offshore floating structures

1 Introduction

The effects of climate change have gained an increasing amount of interest in the last decades, because climate change is a global threat to different aspects of the society, including offshore industry. Offshore floating structures are designed and constructed for exploration and production of oil and gas in a marine environment. During operation stages, they are subjected to environmental loadings, such as wind, wave,

and current. Among them, waves are considered as the dominant loading, because they produce cyclic forces on the structures and usually contribute most to structural damages. Most ocean waves are generated by wind, and wind fields are originally caused by the uneven distribution of global solar radiation which is highly affected by the concentration of greenhouse gases (GHGs). With the emission of GHGs, it is necessary to evaluate the impact of climate change on wave conditions and subsequently on offshore structures.

One widely used approach to evaluate the climate change impact on wave conditions employs statistics. Joint distributions are normally constructed to describe the correlation between wave height and wave period. A long-term linear or quadratic trend of wave height, which is induced by climate change, is considered by modifying the location and scale parameters of joint distributions (Bitner-Gregersen and Haver 1991; Vanem and Bitner-Gregersen 2012). However, statistics cannot entirely reflect the physical process of climate change, and the climate trend is mainly estimated based on the past measurement, ignoring the variation of climate change in the future. Besides, most studies focus on the change of mean wave height and the climate change impact on extreme

✉ Tao Zou
tzou@just.edu.cn

[1] School of Naval Architecture and Ocean Engineering, Jiangsu University of Science and Technology, Zhenjiang, Jiangsu, China

[2] Department of Maritime and Transport Technology, Delft University of Technology, 2628 CD Delft, the Netherlands

environmental conditions, because extreme environmental conditions lead to maximum forces acting on the structures. For example, Young et al. analyzed long-term data of global wave and wind data and concluded that there was a global increasing trend of both wind speed and extreme wave height (Young et al. 2011; Young and Ribal 2019). Bitner-Gregersen et al. investigated the impact of climate change on ultimate strength of tankers by assuming an increase of extreme significant wave height (extreme H_s) with 0.5 m, 1.5 m, and 2.0 m (Bitner-Gregersen et al. 2011). In contrast, the research regarding the climate change effect on fatigue damage is still limited (Bitner-Gregersen and Eide 2010). In structural members and joints of offshore steel floaters, waves produce cyclic stresses. After thousands or millions of stress cycles, small and tiny fatigue cracks may be initiated at these members or joints. Subsequently, these cracks may grow through the thickness. Further crack propagation may even lead to a structural failure.

The calculation of fatigue damage usually requires the wave spectrum for each short-term sea state. DNV-GL recommends a global wave scatter diagram based on decades of observations (DNV-GL-AS 2014). This scatter diagram shows the probability of occurrence of short-term sea states with their significant wave heights and mean periods. Although the observations include the past trend of climate change, they are not exactly representative of the future. In order to investigate the impact of climate change on fatigue damage and improve fatigue design, it is required to "predict" (to be more specific, project) short-term sea states which the offshore structures may encounter in their operational stages. All the projected short-term sea states would then constitute an improved scatter diagram containing the impact of climate change.

Research on climate change has provided deep insight into the mechanism of the climate system (Shine 2010). During recent years, global climate models (GCMs) have been designed to simulate the interactions among atmosphere, ocean, land, and sea ice (Randall et al. 2007). The Earth's climate system is an interactive system which consists of the atmosphere, the hydrosphere, the cryosphere, the land surface, and the biosphere (Baede et al. 2001). It is originally powered by solar radiation. GCMs usually include atmospheric and ocean components. According to their design objectives, some of them also include sea ice and land components as shown in Fig. 1. Basically, the climate change is induced due to external forcing change and internal unforced change. The external forcing change refers to the change of solar radiation on the Earth. It may be caused by the variations of the Sun's output, Milankovitch effect (change of the Earth's orbit and rotation), or the greenhouse effect. For offshore engineering, more attentions should be paid on the emission of GHGs, because the other external forcing factors have much longer time scales (from hundreds to thousands of years) than the greenhouse
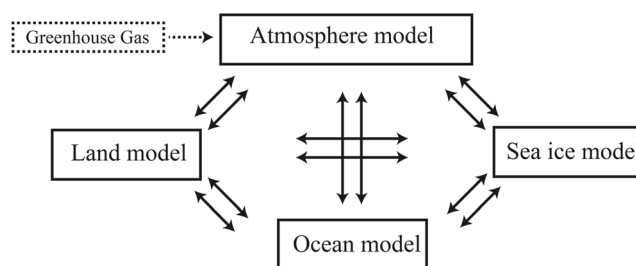

Fig. 1 Components of climate models

effect. Hence, in the following, external forced climate change is represented by the human-induced climate change, because the emission of GHGs is highly affected by human activities. Besides, as the response time of each climate component to external forcing change is different, the internal interactions between the climate components are non-linear, which may induce the internal unforced change (also called natural variability). Therefore, another challenge of this study is that it is still not clear whether the change of wave climate and fatigue damage is mainly induced by internal natural variability or external forced climate change, because the effect of climate change is a combination of both changes (Dobrynin et al. 2015).

By modeling the circulation and interactions of the system components, the response of climate system to the emission of GHGs can be simulated based on climate scenarios. In 2008, 20 climate modeling groups with different climate models participated in the fifth phase of the Coupled Model Intercomparison Project (CMIP5). CMIP5's purpose was to examine the climate's predictability and to explore the models' ability of predicting climate on decadal time scales. Four climate scenarios, named Representative Concentration Pathways (RCPs), were selected and defined as the driving force of climate models (van Vuuren et al. 2011). RCPs project the radiative forcing trajectories and describe a wide range of the main drivers for climate change from the year of 2000 to 2100. These drivers include greenhouse gas, air pollutant emissions, and land use. Based on climate scenarios, the climate change in the future may become predictable, especially on large spatial scales (Baede et al. 2001). Climate scenarios should not be viewed as accurate predictions of the future climate. Instead, each of them only represents one possibility of the future based on a set of prior expectations.

Although there are ocean components in GCMs, the simulations of ocean surface waves are not incorporated. In fact, wave modeling research has a long history which can be traced back to 1886 (Greenhill 1886). At that time, analytical methods were mainly used to simulate ocean waves. The modern study of ocean surface waves started with a pioneer study by Sverdrup and Munk (1952). Hasselmann et al. (1985) presented a discrete-interaction operator parameterization which improved the development of the third-generation wave models. The third-generation wave models, driven by

wind forces, can numerically simulate wind-wave interactions, nonlinear wave-wave interactions, and energy dissipation (Tolman et al. 2002). The most widely used wind-driven wave models are Ocean Wave Model (WAM), Simulating WAves Nearshore model (SWAN), and WaveWatch-III (WW3) model (Tolman 2014). Hemer et al. (2013) and Morim et al. (2019) projected the global trend of wave climate by coupling wave model to climate models. The wind-driven wave model is normally used to simulate short-term sea states and has been applied in many other fields, such as coastal engineering, wave energy harvesting, wave forecasting and hindcasting, and fatigue calculations (Booij et al. 1999; Gómez Lahoz and Albiach 2005; Rusu and Guedes Soares 2009; Zou and Kaminski 2016).

This paper aims to project the effect of climate change on fatigue damage of offshore floating structures in the North Sea and to evaluate whether human activities (GHG emissions) considerably affect the wave climate and fatigue damage in decadal time scales. The methodology of projecting the climate change impact is introduced in the following section. Three oil fields in the North Sea are selected to demonstrate this methodology. The effects of sea ice melting and sea level rising are not considered. Waves are viewed as the only source of fatigue damage. The other sources such as wind, current, loading, and offloading have been disregarded.

2 Methodology

2.1 Climate scenarios, global climate, and wave models

In this study, the climate scenario Representative Concentration Pathway 8.5 (RCP8.5) was selected to project the future climate conditions to exemplify the extreme response of climate system, because it is characterized by high GHG emissions and radiative forcing level (Riahi et al. 2011). It was constructed with the spatial resolution of approximately 60 km and the temporal resolution of 1 year. The temporal resolution can be modified to monthly, daily, or even 6 hourly, based on the seasonal cycle and the historic radiative data.

The global wind fields were simulated by Centro Euro-Mediterraneo sui Cambiamenti Climatici Climate Model (CMCC-CM), and all the wind data were obtained from the CMIP5 database (Scoccimarro et al. 2011). CMCC-CM is a coupled atmosphere–ocean global circulation model. The atmospheric component is ECHAM5 (Roeckner et al. 2003) with the grid resolution $0.75° \times 0.75°$. The ocean component is the global ocean model OPA 8.2 (Madec et al. 1998) in its ORCA2 global configuration with the grid resolution $2° \times 2°$. There are 31 vertical layers in ECHAM5 with the top layer at 10 hPa (approximately 31,055 m's altitude) and 31 vertical layers in OPA 8.2 with 10 layers below the 100-m surface

altitude. The interaction between the atmospheric and oceanic model is calculated every 160 min based on the Ocean Atmosphere Sea Ice Soil version 3 (OASIS3) coupler (Valcke 2013).

The 6-hourly surface wind data simulated by CMCC-CM were used to run the wind-driven surface wave model WaveWatch-III. The wave modeling area covers a region of 0°–80° N/60° W–20° E latitude/longitude. The swells coming from outside the model region are neglected, because they have limited impact on the structural fatigue damage. The spatial boundaries are set as land points which block the transport of wave energy and limit the interaction between water surface and wind. The short-term sea states simulated by the wave model are represented by 6-hourly wave spectra defined for 24 directions (i.e., every 15°) and 25 frequencies ranging from 0.042 Hz to 0.414 Hz. The wave condition at each spatial grid was partitioned into multiple wave systems (one wind wave and one or two swells) by wave spectra partitioning (Janssen 2008). More details of modeling are listed in Table 1. The setup of wave modeling has been validated by comparing the wave data with the buoy measurement in the sea area offshore South Africa (Zou and Kaminski 2016). By coupling wave models to climate models, the fatigue analysis for offshore floating structures can be conducted as shown in Fig. 2.

2.2 Floating structures in the North Sea

The North Sea is a mature oil and gas producing region. The exploitation of the North Sea oil reserves began in the 1970s. Due to its high oil quality and the political stability, a lot of oil fields have been discovered and exploited. However, with the decrease of output in shallow oil fields, more oil fields in deep water are exploited, which requires more floating offshore structures. In this paper, three North Sea oil fields were selected, Rosebank, Alma/Galia, and Pierce (see Fig. 3), to evaluate the climate change impact on their wave conditions. The fields Alma/Galia (56.2° N; 2.8° E) and Pierce (58° N; 1.45° E) are both in the central North Sea with a water depth of

Table 1 The modeling details

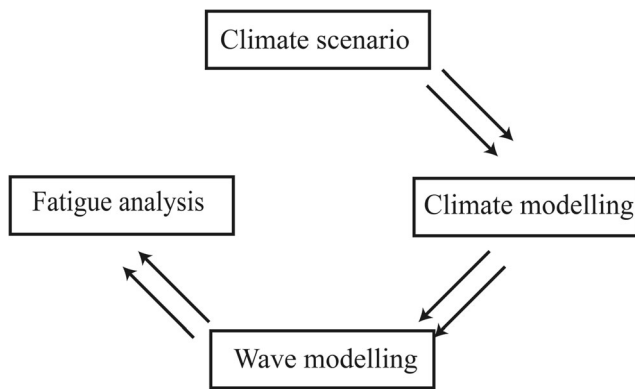|	
Climate scenario	RCP8.5
Climate model	CMCC-CM
Wave model	WaveWatch-III
Spatial resolution	$0.75° \times 0.75°$
Global time step	3600 s
Source-term time step	300 s
Topography	ETOPO1
Model output	6-hourly wave data

Fig. 2 Flow chart of methodology

approximately 100 m. Rosebank oil field (61° N; 4° W) is located North-West of the Shetland Islands with a water depth of approximately 1100 m.

The Floating Production, Storage and Offloading unit (FPSO) Glas Dowr is assumed to be operating in these three oil fields. Glas Dowr is a converted turret FPSO owned by Bluewater. Since the turret allows the vessel to rotate, the relative wave directions of wave partitions are calculated by vessel heading analysis as shown in Fig. 4. The vessel heading is always opposite to the direction of mixed wave. The mixed wave is partitioned into three wave systems: one wind wave and two swells. The vector of mixed wave is the sum of all wave system vectors. The methodology of this paper is suitable for all the oceans in the world and all types of floating structures. The North Sea and Glas Dowr were just selected to exemplify the method.

2.3 Projected simulations and control simulations

Based on RCP8.5, the surface wind data in the North Sea for the present, near-future, and far-future decades (2011–2020, 2051–2060, and 2091–2100) were obtained from CMCC-CM simulations (Scoccimarro et al. 2011). The trend of surface wind speed in the North Sea is projected as shown in Fig. 5. With the wind driving force, the sea states in North Sea were projected by WaveWatch-III. This process is called projected simulations. The initial wave conditions and boundary conditions are obtained by simulating the sea states 1 year earlier than the projected periods. Then, the annual significant wave heights (H_s) in the selected oil fields were calculated. There is a negative trend of annual H_s over time in all three oil fields as shown in Fig. 6a–c. H_s decreased by approximately 0.5 m from 1850 to 2100. Considering that the North Sea is a wind-wave-dominated sea area, this decrease is in agreement with the earlier findings (Bitner-Gregersen et al. 2011; Dobrynin et al. 2015). These earlier findings reveal that the overall wind speed in the North Sea is decreasing with the emission of GHGs over time. Furthermore, the averaged wave height of Rosebank oil field is higher than the other oil fields, and the averaged wave heights in Alma/Galia and Pierce oil fields are close to each other, as listed in Table 2. Rosebank has the highest wave height, because it is also vulnerable to waves from the North Atlantic Ocean.

The variability of annual significant wave height is attributed to both human-induced climate change and unforced natural variability. In order to evaluate the effect of natural variability, the output of a 30-member ensemble analysis from
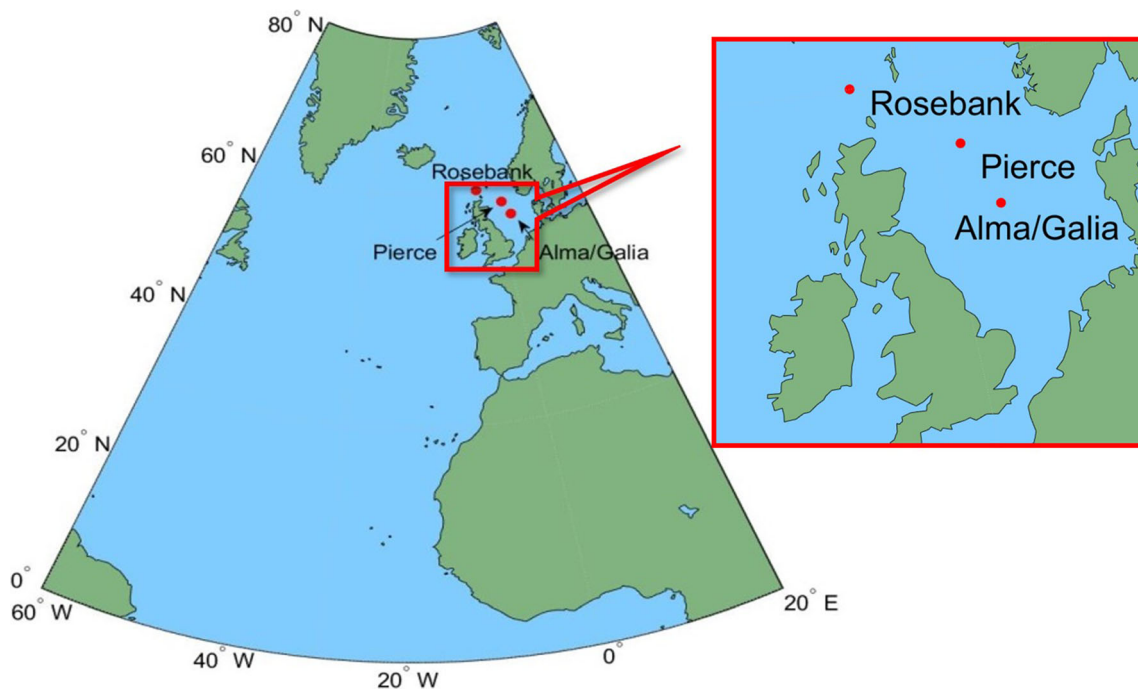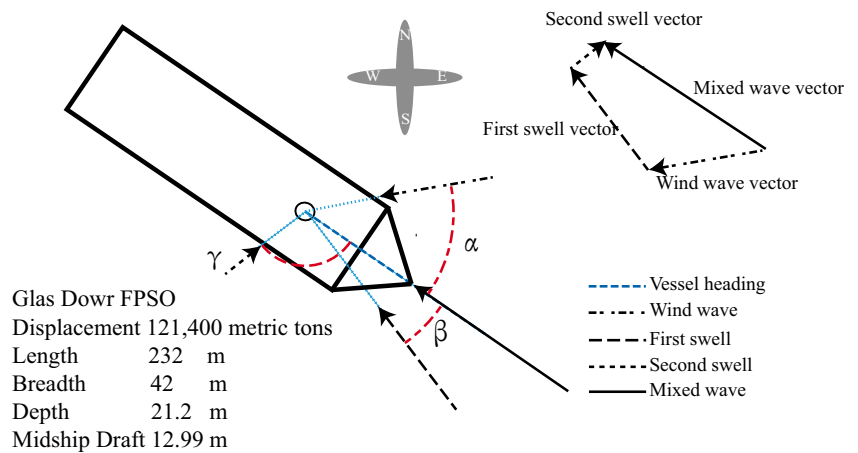

Fig. 3 Geographical locations of three oil fields in the North Sea. The wave modeling area covers a region of 0°–80° N/60° W–20° E latitude/longitude

Fig. 4 The main characteristics of Glas Dowr and the demonstration of vessel heading analysis. The relative directions of wave component systems are defined as α, β, and γ to calculate fatigue damage

CMIP5 was used to run WaveWatch-III. This ensemble analysis was carried out under constant unforced preindustrial climate conditions (the solar radiation and GHG concentrations for 1850). The sea states under the constant climate conditions were simulated as shown in Fig. 6d. In this simulation, the radiative forcing was "controlled" so that the variability of sea states between each year was induced only by unforced natural variability. This ensemble analysis is also called the control simulation below.

2.4 Detection of human-induced climate change impact on wave conditions

The sea states are simulated through WaveWatch-III with the driven wind data from the 30-member control simulation. There are 1460 (4 × 365 days) continuous 6-hourly sea states simulated by WaveWatch-III for each ensemble member with a duration of 1 year. These 6-hourly sea states are indexed by two indices: an index n to denote an ensemble number with $n = \{1,2,\ldots, 30\}$ and an index m to denote a successive sea state number with $m = \{1,2,\ldots,1460\}$. The mth sea state in the nth ensemble member is represented by the indicator $n - m$. For each oil field, all the 6-hourly sea states in the control

simulation were subsampled with different sample lengths (ranging from 1 to 10 years). The sampling was conducted by shifting the sample length with a constant time increment of 6 h (the length of one sea state) over successive sea states (Fig. 7). Overlapping samples were allowed (Fig. 8). As a result, the sample size for each sample length is ranging from 42,341 to 29,200 (i.e., the number of sampling unit for each sample length is from 42,341 to 29,200). The averaged significant wave height of sampling units in the same sample length was fitted by the normal distribution $N(\mu_i, \sigma_i)$, $i=\{1,2,,\ldots, 10\}$ (i is corresponding to each sample length). Since the variability of sea states in the control simulation was induced by natural variability, the range of natural variability of H_s was estimated by confidence intervals. The 0.05 and 0.95 confidence intervals were calculated as the lower and upper boundaries of natural variability (the dotted red and blue lines in Fig. 9).

The next step is to detect the effect of human activities (GHG emissions) on sea states. Based on RCP8.5, the sea states in the North Sea of three decadal periods were projected. For the present decade (2011–2020), the averaging significant wave height $H_{sa}(t)$ for each sampling length $t = \{1; 2; \ldots; 10\}$ was calculated as follows:

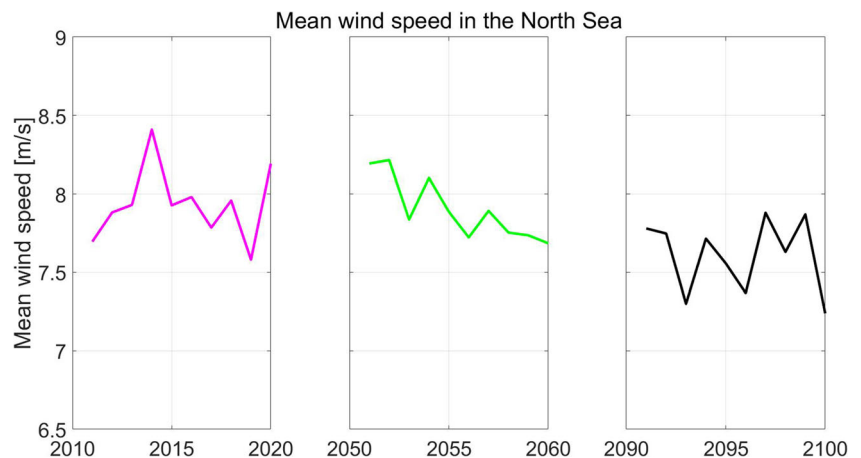**Fig. 5** Trend of mean surface wind speed over the North Sea

Fig. 6 Variability of annual significant wave height at the selected oil fields. The dotted blue lines are the averaged significant wave height and the 95% confidence interval in the control simulation
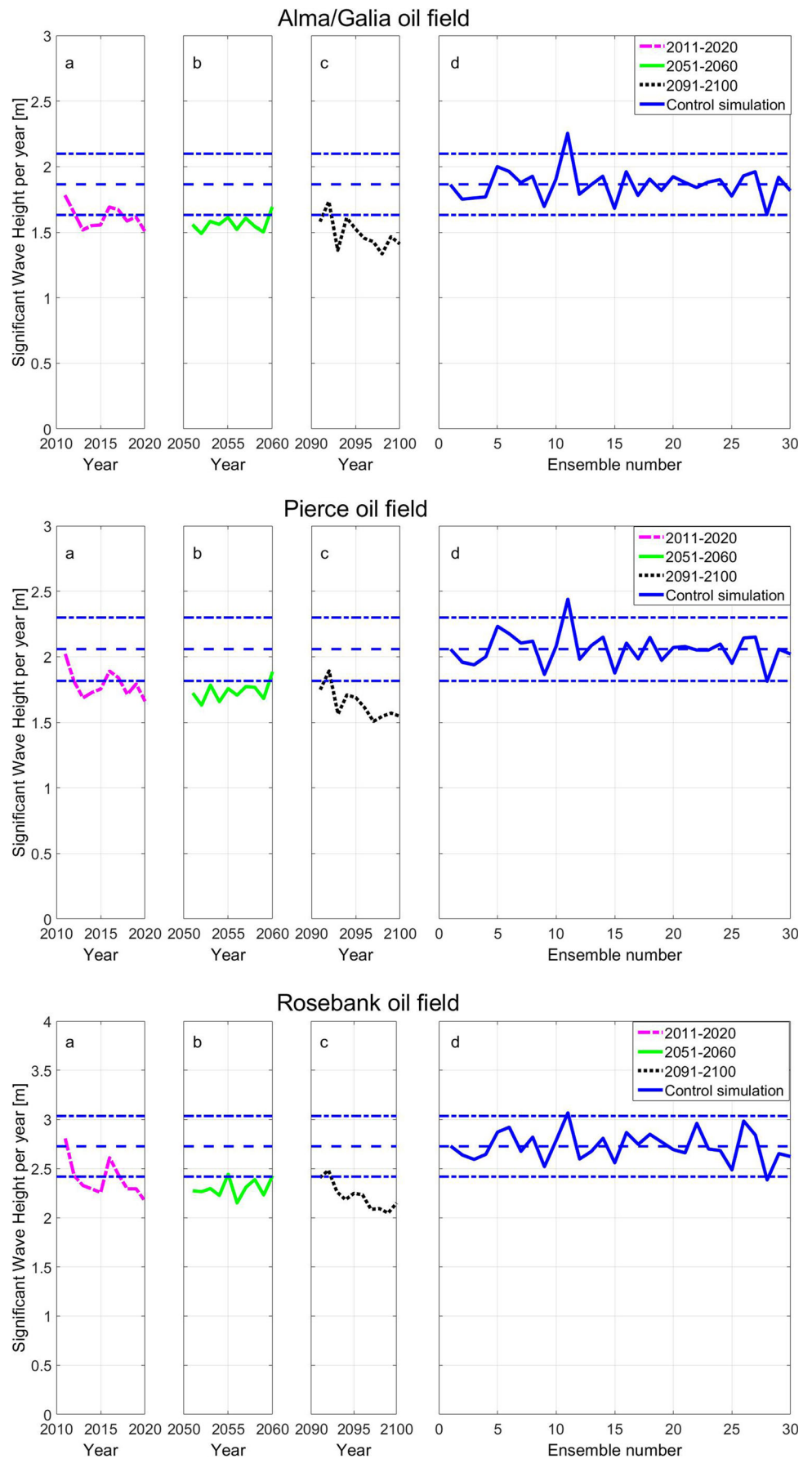
Table 2 Averaged significant wave height under the projected simulations

Oil fields	Alma/Galia	Pierce	Rosebank
Averaged significant wave height (m)	1.56	1.72	2.30
Standard deviation (Std) (m)	0.12	0.12	0.15

$$H_{sa}(1) = H_s(2011) \tag{1}$$

$$H_{sa}(2) = H_s(2011-2012) \tag{2}$$

$$H_{sa}(3) = H_s(2011-2013) \tag{3}$$

$$H_{sa}(10) = H_s(2011-2020) \tag{4}$$

where $H_s(p)$ is the averaged significant wave height within the time period $p = \{2011; 2011 - 2012; 2011 - 2013; \cdots; 2011 - 2020\}$. For the other two decades (2051–2060 and 2091–2100), the averaging significant wave height $H_{sa}(t)$ was calculated in the same way as listed in Eqs. (1, 2, 3, and 4).

Then, for each decadal period, $H_{sa}(t)$ was compared with the upper and lower boundaries of natural variability (see Fig. 9). It can be seen that the trajectories of projected wave height exceed the lower boundary when the sampling length exceeds 2 years. This time length is defined as the detection period. It indicates that the impact of human activities on wave conditions is statistically significant and the human-induced climate change is detected.

In addition, when the sampling length is 1 year, the sampling data has the highest dispersion which is caused by natural variability. It indicates that the natural variability may significantly affect the simulations over short periods, and the result of these simulations would include a high level of randomness. With the increase of sampling length, the

dispersion of significant wave height is getting smaller, because the variation in 1 year is compensated for by the opposite variation in another year. The significant wave height of the 6-hourly sea states is defined as a normally distributed variable, written as $H_s \sim N(\mu_s, \sigma_s)$. All the sea states are considered independent. In each sampling unit, the number of all sea states is n, and their averaged significant wave height is defined as $\overline{H}_s \sim N(\overline{\mu}_s, \overline{\sigma}_s)$. Then, μ_s is very close to $\overline{\mu}_s$, because they are from the same population. The standard deviation of $\overline{H}_s$ is the standard deviation of H_s for each individual sea state divided by the square root of sea state number n:

$$\overline{\sigma}_s = \frac{\sigma_s}{\sqrt{n}} \tag{5}$$

where n is increasing with the length of sampling length. As a result, with the increase of sampling length, the range of natural variability is becoming narrower, and its effect is getting less pronounced.

Since the calculations of fatigue damage are more time-consuming than simulating sea states, the sea state data from the control simulation were also subsampled with a long-time increment to reduce the amount of fatigue computations. The primary difference was that the constant time increment increased to 1 year instead of 6 h as shown in Fig. 10 and Fig. 11. In this case, the sample size was significantly decreased to 30 for 1-year samples and 21 for 10-year samples. This sampling approach can effectively reduce the calculation time, but may also induce more uncertainties into the calculations.

With the 1-year time increment, the range of natural variability is not significantly changed. The trajectories of projected wave height also exceed the lower boundary, and the detection period is 1 or 2 years (Fig. 12) which is equal to those in Fig. 9. The detection period is very short, because there are more than 160 years between the control simulation
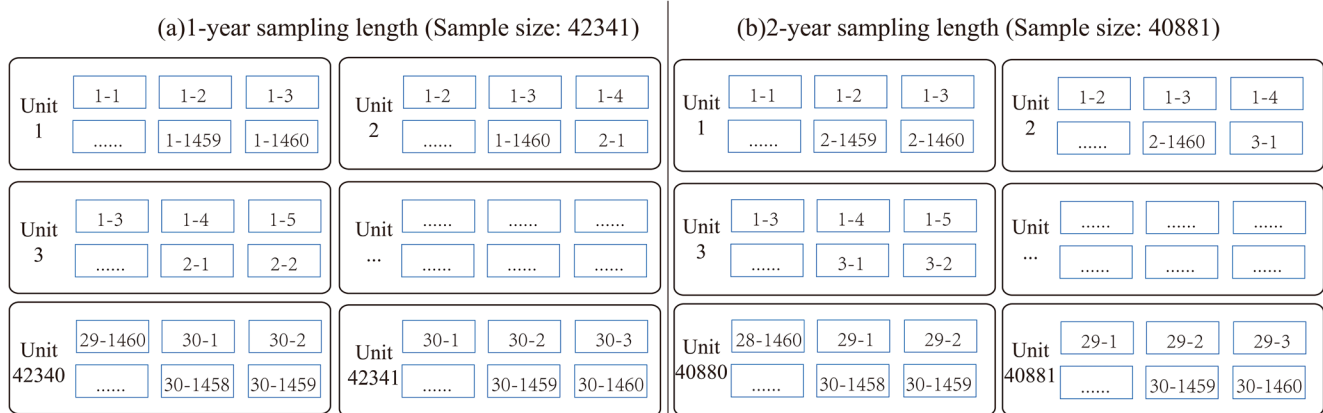

Fig. 7 Sampling result with 6-h time increment. The sampling results for 1-year and 2-year sample length are listed here to exemplify the sampling approach. For the other sample lengths (from 3 years to 10 years), the results are not shown. Each 6-hourly sea state is represented by the indicator $n - m$ in the blue boxes. The black boxes stand for the sampling units in each sample
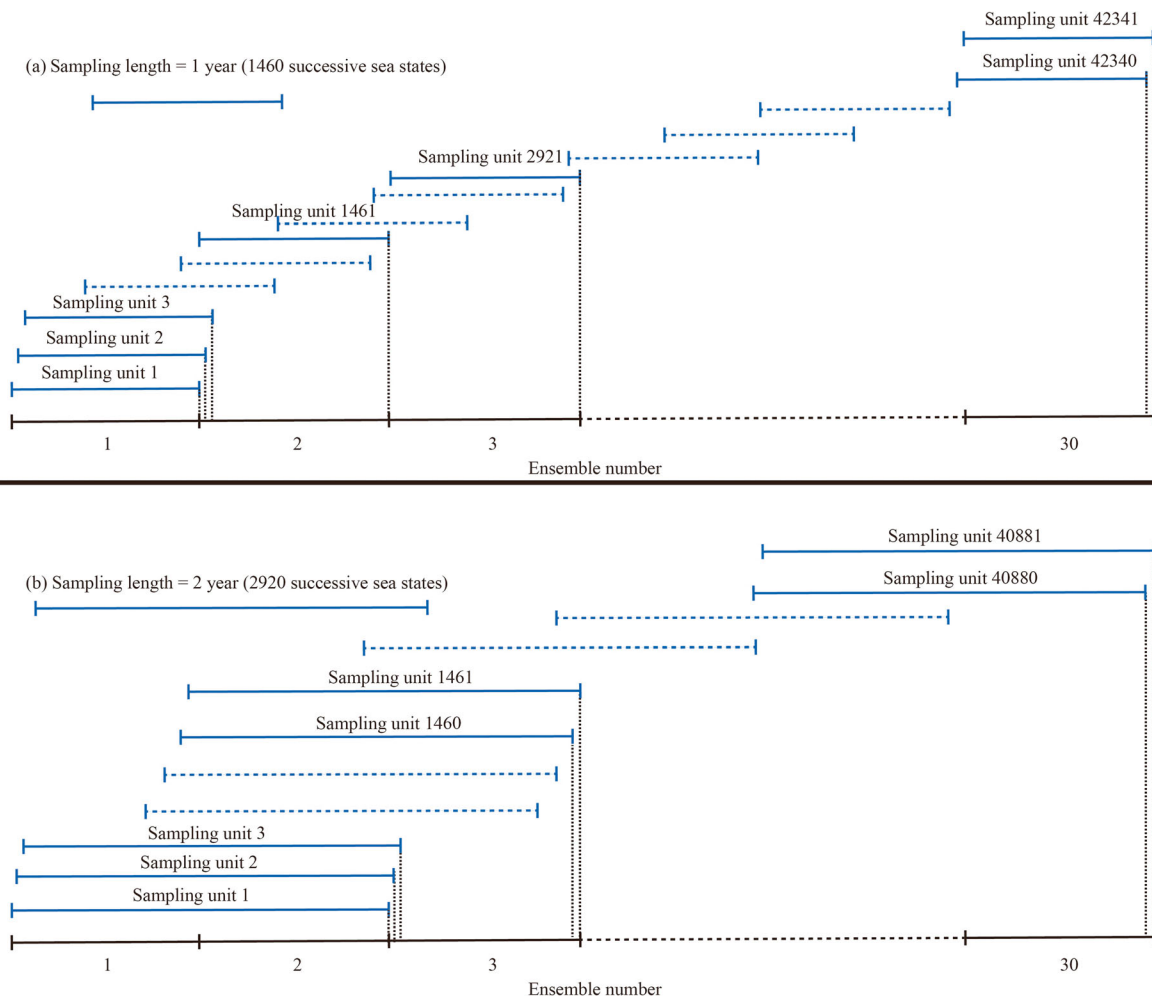
Fig. 8 Illustration of overlapping samples with 6-h time increment. Neighboring units overlap with each other by (**a**) 1459 sea states and (**b**) 2919 sea states. Most sampling units are not shown in order to simplify the plot

and the projected simulation. The climate change is a cumulative process. Within 160 years, the effect of climate change on sea state has become very pronounced. As a result, the change of time increment from 6 h to 1 year does not significantly affect the standard deviation of samples which is important to estimate the range of natural variability, as listed in Table 3. Hence, it is recommended to use the 1-year time increment to sample data for the following fatigue calculations, because it can limit the sample size and reduce the amount of calculations. In short, no matter which sampling time increment is applied, there is a clear exceedance of the projected wave height over the boundaries. The detection period in all three oil fields is shorter than the detection period of other studies (Dobrynin et al. 2015). This difference could be explained by the fact that the present study focuses on a single location (three specific oil fields), whereas other studies focus on the average climate change over large areas. A decreasing trend at one location can be compensated by an increasing trend in other neighboring locations.

2.5 Detection of human-induced climate change impact on fatigue damage

In this study, the fatigue damage on the main deck of FPSO Glas Dowr at frame 66½ above decks longitudinal #22 (location No.1 in Fig. 13) was calculated by software Bluefat. The structural main characteristics are listed in Fig. 4. Bluefat is a component of an advisory monitoring system Monitas (Aalberts et al. 2010; Kaminski and Aalberts 2010). Simple beam models were used to calculate the structural response. There are four loading mechanisms considered: overall vertical and horizontal bending of the vessel, local bending of secondary stiffeners caused by external action of waves (including a correction for the intermittent wetting effect), and internal tank pressure fluctuations induced by varying motions of the FPSO. By using the wave partitioning technique (Hanson and Phillips 2001), the scatter diagrams of wave systems (wind wave and

Fig. 9 The natural variability of significant wave height and the detection of human-induced climate change (6-h time increment). The shadowed area represents the range of natural variability estimated by the control simulation. The solid lines are the averaged significant wave heights for 2011–2020 (green), for 2051–2060 (blue), and for 2091–2100 (red). They are calculated by projected simulations with RCP8.5. The horizontal straight dotted line is the averaged significant wave height in the control simulations for each sampling length
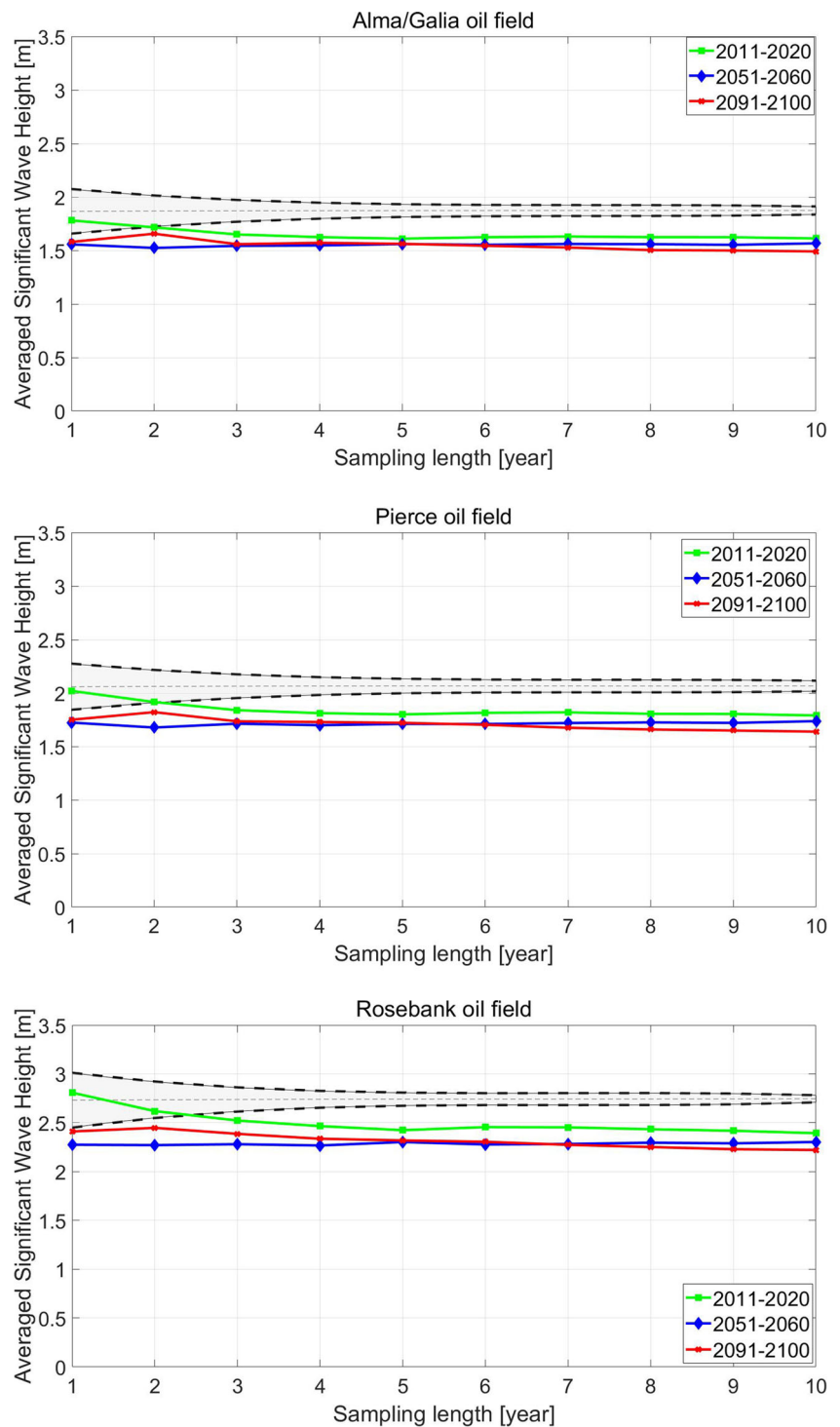
swells) were generated by WaveWatch-III. Then, Bluefat calculated the wave-induced fatigue damage with the conventional spectral fatigue calculation method.

In the spectral fatigue calculations, the key environmental parameters are wave height, period, and directions to describe wave spectra. Since we are using a linear method to calculate

fatigue damage as Eq. (1), the relationship between the structural response and the wave conditions is represented by the response amplitude operator (RAO).

The stress response spectrum and spectral moments in linear models are defined as

$$S_\sigma(\omega|H_s, T_z, \theta) = |H_\sigma(\omega|\theta)|^2 \cdot S_\eta(\omega|H_s, T_z) \qquad (6)$$
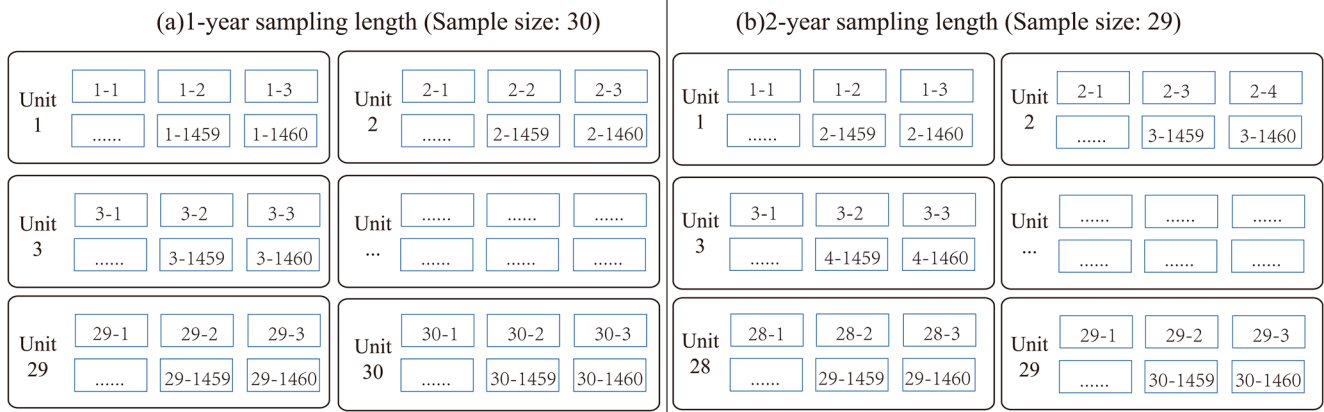
Fig. 10 Sampling result with 1-year time increment. The sampling results for 1-year and 2-year sample length are listed here to exemplify the sampling approach. For the other sample lengths (from 3 to 10 years), the results are not shown. Each 6-hourly sea state is represented by the indicator $n - m$ in the blue boxes. The black boxes stand for the sampling units in each sample

$$m_n = \int_\omega \sum_{\theta-90^\circ}^{\theta+90^\circ} f(\theta)\omega^n \cdot S_\sigma(\omega|H_s, T_z, \theta)\mathrm{d}\omega \qquad (7)$$

where $H_\sigma(\omega|\theta)$ is the transfer function which represent the relation between unit wave amplitude and response (see Fig. 14), $|H_\sigma(\omega|\theta)|^2$ is the response amplitude operator, $S_\eta(\omega|$

$H_s, T_z)$ is wave spectrum, and $f(\theta)$ is the wave spreading function. It can be seen that the maximum vertical bending moment in head sea conditions is higher than the moment in the other conditions. In head sea conditions, the transfer function curve reaches its peak when the wave length is approximately equal to the ship length due to hogging and sagging. For a
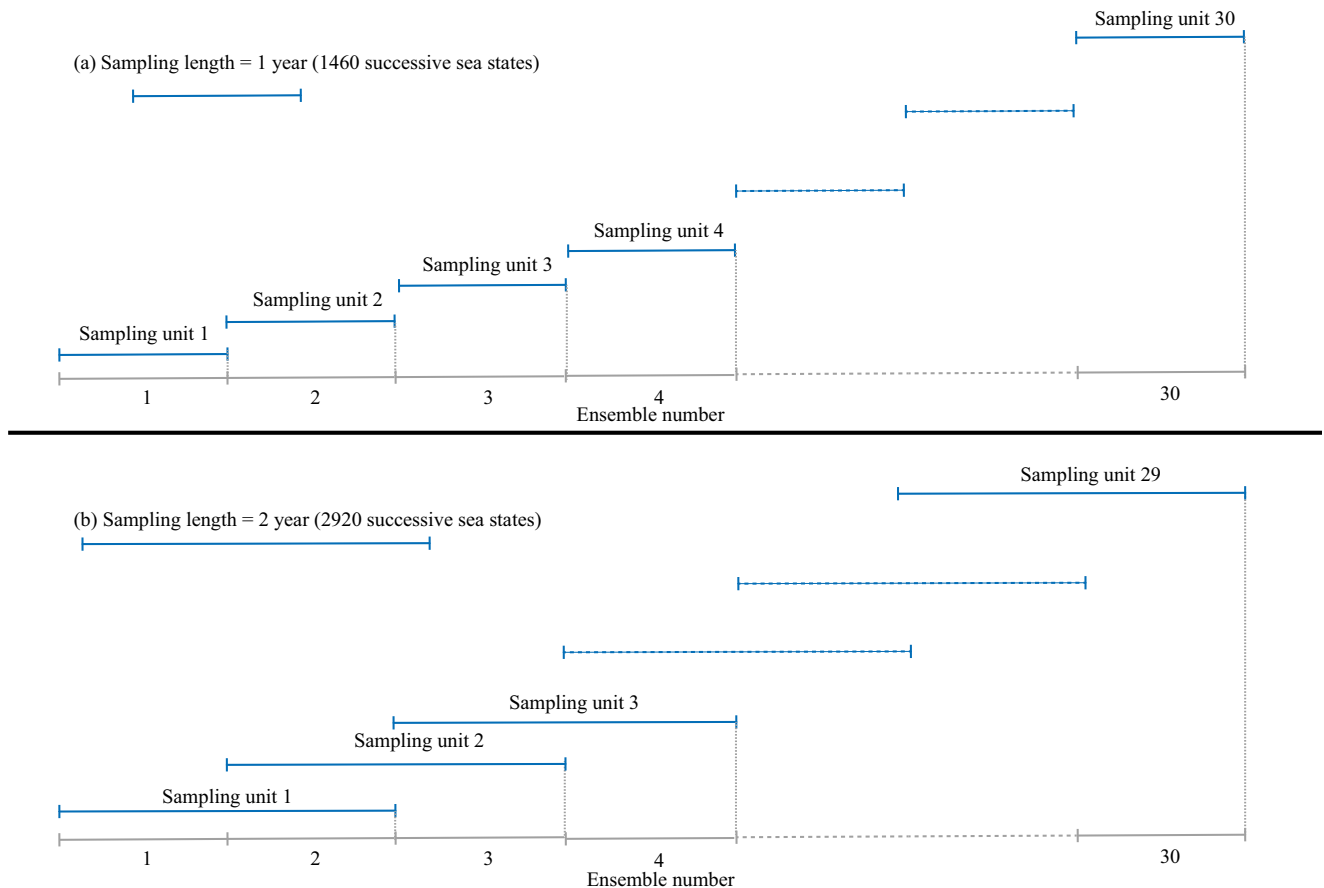

Fig. 11 Illustration of overlapping samples with 1-year time increment. Neighboring units overlap with each other by (a) 0 sea states and (b) 1460 sea states. Most sampling units are not shown in order to simplify the plot

Fig. 12 The natural variability of significant wave height and the detection of human-induced climate change (1-year time increment). The shadowed area represents the range of natural variability estimated by the control simulation. The solid lines are the averaged significant wave heights for 2011–2020 (green), for 2051–2060 (blue), and for 2091–2100 (red). They are calculated by projected simulations with RCP8.5. The horizontal straight dotted line is the averaged significant wave height in the control simulations for each sampling length
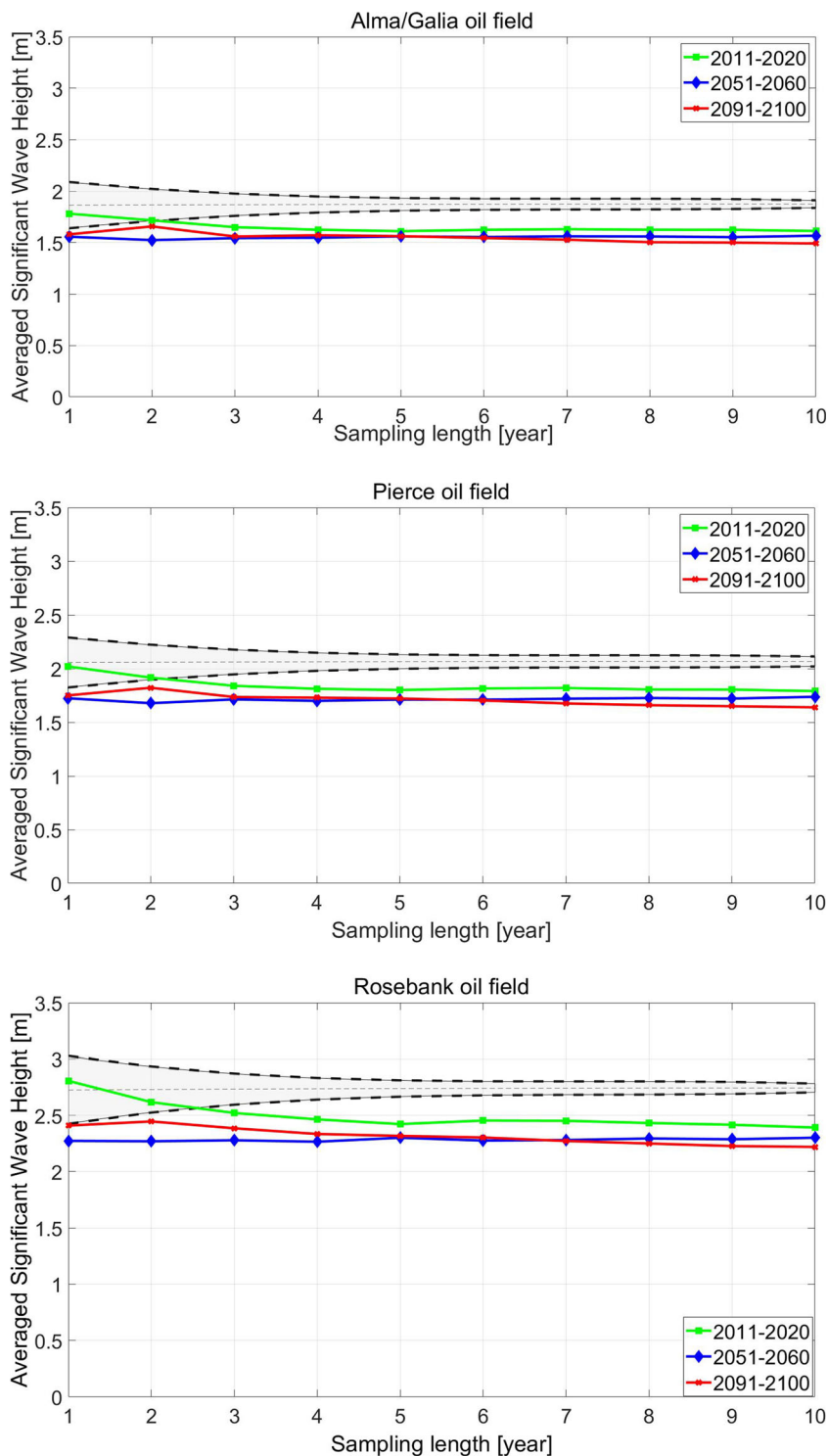
particular offshore structure, the fatigue damage is mainly determined by sea states which are represented by wave scatter diagrams. We use one wave spectrum (represented by its significant wave height, crossing period, and primary direction) to represent one 6-hourly wave condition.

Once the stress response spectra are calculated for each 6-hourly sea state, the wave-induced fatigue damage can be calculated through SN curves, as shown in Fig. 15 and Eq. (8). A SN Curve is a plot of the range of cyclic stress versus the number of cycles to fatigue failure for a given material.

$$\log(S) = A + m \cdot \log(N) \tag{8}$$

where S is the stress range, N is number of cycles when a fatigue failure occurs, and m and A are constants.

Table 3 The standard deviation of significant wave height in the control simulation

	Time increment	Sampling length (year)									
		1	2	3	4	5	6	7	8	9	10
Alma/Galia (m)	6 h	0.107	0.072	0.050	0.039	0.030	0.026	0.026	0.025	0.022	0.020
	1 year	0.117	0.074	0.054	0.043	0.031	0.027	0.026	0.025	0.023	0.019
Pierce (m)	6 h	0.111	0.076	0.054	0.045	0.034	0.030	0.030	0.029	0.028	0.026
	1 year	0.121	0.079	0.058	0.046	0.034	0.029	0.029	0.028	0.026	0.024
Rosebank (m)	6 h	0.145	0.092	0.059	0.047	0.034	0.032	0.032	0.028	0.025	0.020
	1 year	0.154	0.102	0.071	0.049	0.034	0.034	0.032	0.027	0.024	0.021

The one-slope SN curve with $m = 3$ and $a = 12.76$ (stresses in MPa) was used to represent the fatigue resistance, and the fatigue damage is calculated by the equation below (DNV-GL-AS 2014):

$$D = \frac{\omega_0 T_d}{a} \Gamma\left(1 + \frac{m}{2}\right) \sum_{n=1}^{N_{load}} p_n \sum_{i=1, j=1}^{\text{all seastates}} r_{ijn}\left(2\sqrt{2m_{0ijn}}\right)^m \tag{9}$$

where D is accumulated fatigue damage, ω_0 is the average long-term zero-crossing frequency, a and m are the S-N curve parameters, T_d is the design life of the structure, Γ is the gamma function, N_{load} is the total number of load conditions, p_n is the fraction of the design life in load condition n, r_{ijn} is the relative number of stress cycles in short-term condition i and j, and m_{0ijn} is the zero spectral moment of stress response process.

The range of natural variability of annual fatigue damage was estimated using the sea states obtained from the control simulations. As fatigue calculations were very time-consuming, the sampling time increment was set to 1 year rather than 6 h in order to reduce the amount of calculations. Then, based on RCP8.5 climate scenario, the annual fatigue damages for the present, near-future, and far-future decades were calculated using the sea states from projected simulations. The annual fatigue damages in the three oil fields are all decreasing, and there is a considerable impact of human-induced climate change on annual fatigue damage as shown in Fig. 16. The detection period is 1–2 years equal to that of H_s. It means when the dominant wave characteristic (wave height) has a considerable change, the other wave properties can hardly affect the detection period.

2.6 Discussion

In this paper, the effects of climate change on wave height and fatigue damage are investigated. The fatigue damage is mainly induced by wave loadings, but it is more sensitive to climate change than wave height. As seen in Tables 4 and 5, the bias of fatigue damage (0.30–0.62) is much lower than the bias of wave height (0.80–0.88). It means the fatigue damage is decreasing faster than wave height. In addition, the change of

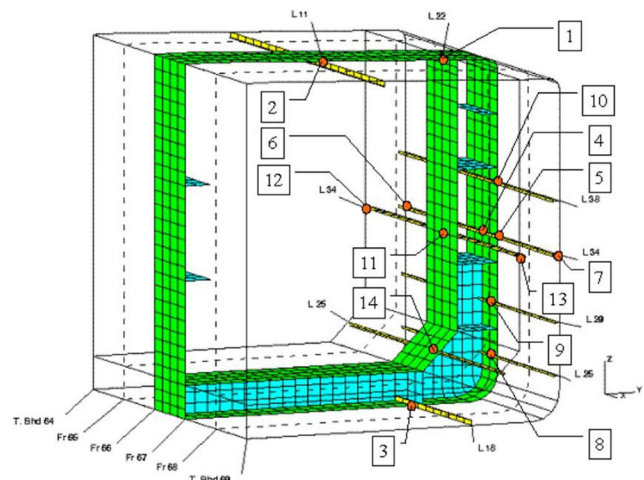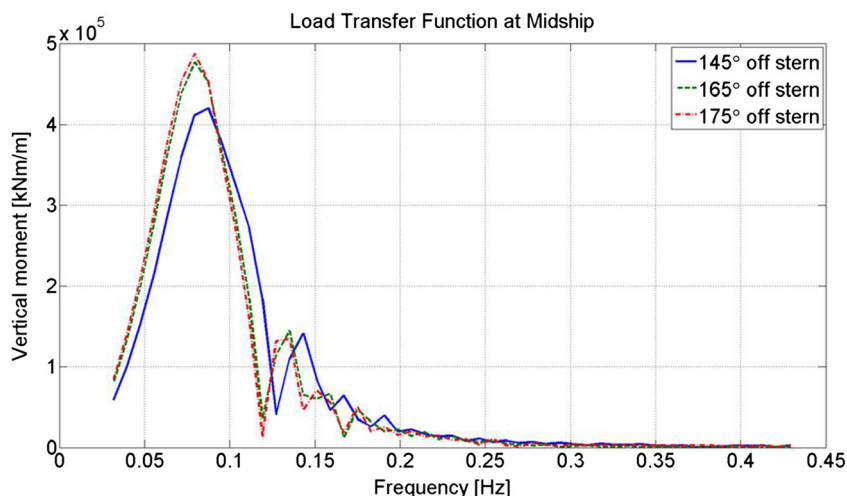**Fig. 13** FPSO-Glas Dowr and its midship section

Fig. 14 Load transfer function

fatigue damage is not only decided by wave height but also the other wave characteristics, such as wave periods, wave directions, and their distributions. In the linear structural model, the structural response is proportional to the wave forces. Hence, when the inverse slope of S-N curves is equal to 3, the fatigue damage is approximately proportional to the third power of wave height as listed in Eq. (6). When the bias of wave height is ranging from 0.80 to 0.88, the bias of fatigue damage should be roughly ranging from 0.51 to 0.68. However, this estimated bias of fatigue damage is higher than this calculated value in Table 5. It reveals that although wave height is the dominant wave characteristic in fatigue calculations, it is still necessary to consider the change of wave period and wave direction in fatigue calculations. Among all three oil fields, Rosebank has the highest bias of fatigue damage

(0.45–0.62), which is also the closest to the estimated fatigue bias (0.51–0.68). It is because Rosebank has the highest wave height than the other two oil fields, and wave height is more dominant in fatigue calculations than the other wave characteristics. The changes of wave periods and directions in Rosebank contribute less to the change of fatigue damage.

3 Conclusions

This study projected the fatigue damage of an FPSO in the North Sea by coupling climate models to wave models and also detected the considerable impact of human-induced climate change. The sea states for the present, near-future, and far-future decades in three oil fields were projected based on RCP8.5 climate scenario.
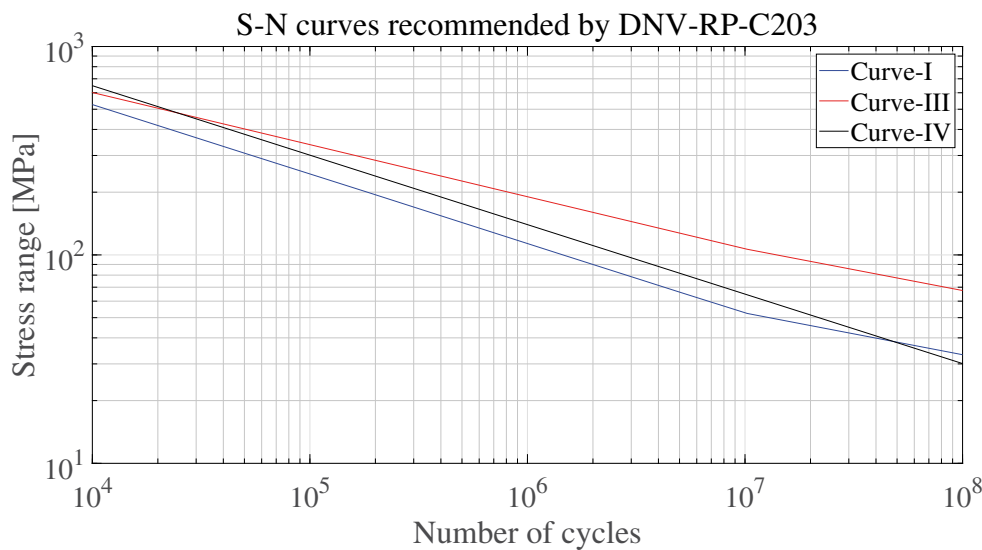
Fig. 15 SN curves

Fig. 16 The natural variability of annual fatigue damage and the detection of human-induced climate change (1-year time increment). The shadowed area represents the range of natural variability calculated by the control simulation. The solid lines are the annual fatigue damages from 2011 to 2020 (green), from 2051 to 2060 (blue), and from 2091 to 2100 (red). The horizontal straight dotted line is the average annual fatigue damage in the control simulations for each sampling length
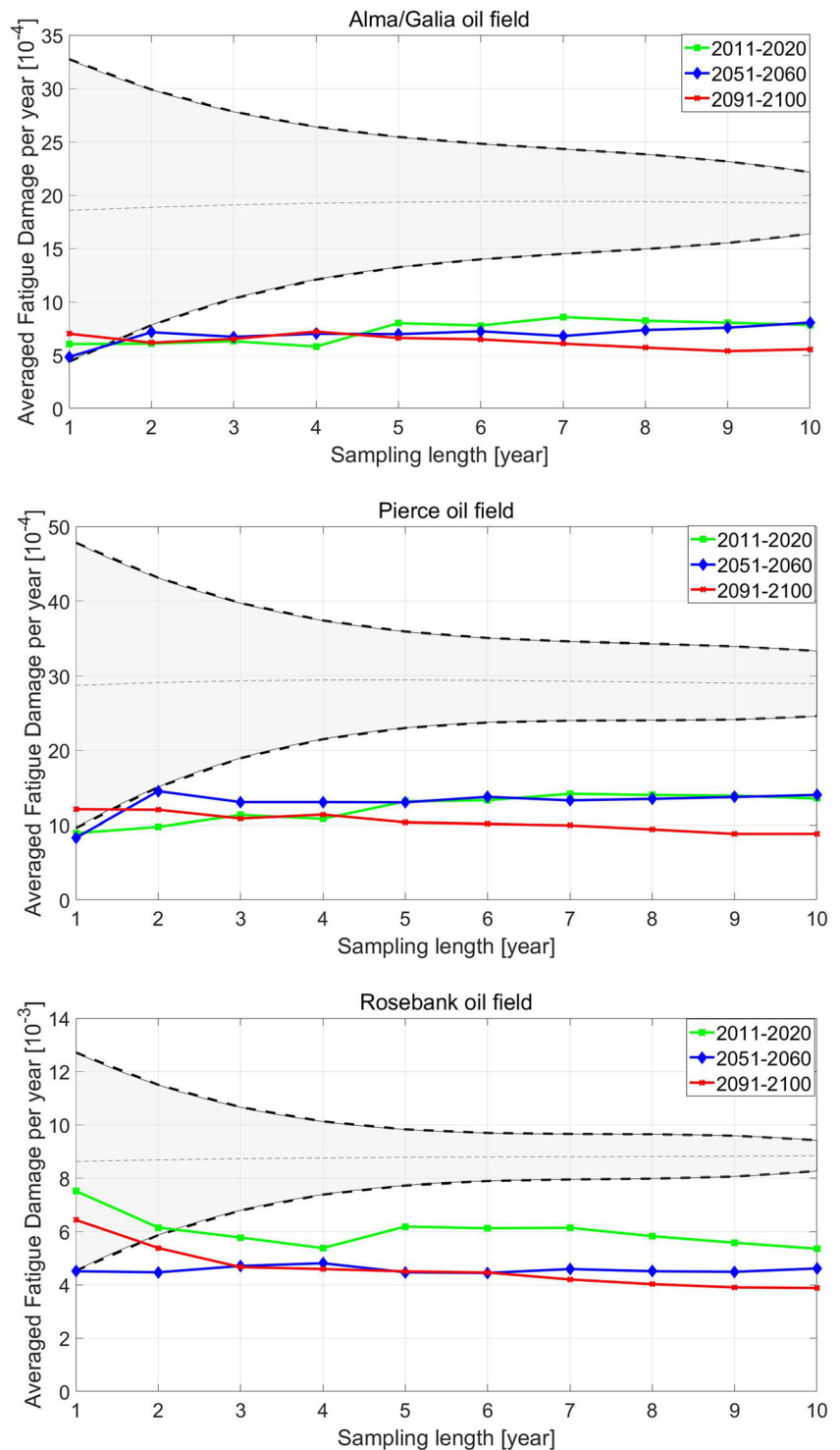
The result confirms that the significant wave height in the North Sea is decreasing with the emission of GHGs and the rate of wave change is region-dependent. The sea states are getting calmer and making less fatigue damage. It indicates that some fatigue lifetime reserve will be present for the floating structures in the North Sea providing the climate change has not been taken into account in their design. The downward trends of significant wave height and fatigue damage are similar. However, the trend of wave height can not completely represent the trend of fatigue damage, because, in addition to wave height, the other wave characteristics, such as wave period or relative wave direction, also affect fatigue damage. The methodology presented in this

Table 4 Comparison of H_s in three oil fields

Oil field	Simulations	Time year	Mean m	Std m	CV* -	Bias** -
Rosebank	Control	1850–1879	2.72	0.15	0.06	-
	RCP85	2011–2020	2.39	0.19	0.08	0.88
		2051–2060	2.30	0.09	0.04	0.84
		2091–2100	2.22	0.14	0.06	0.81
Alma/Galia	Control	1850–1879	1.86	0.12	0.06	-
	RCP85	2011–2020	1.61	0.09	0.06	0.86
		2051–2060	1.57	0.06	0.04	0.84
		2091–2100	1.49	0.12	0.08	0.80
Pierce	Control	1850–1879	2.06	0.12	0.06	-
	RCP85	2011–2020	1.79	0.11	0.06	0.87
		2051–2060	1.74	0.07	0.04	0.84
		2091–2100	1.64	0.12	0.07	0.80

*Coefficient of variation (CV) expresses the extent of variability in relation to mean value. A higher CV stands for a higher variation

**The bias has been defined as the ratio between the mean value from the projected simulations and the mean from the control simulations

paper allows considering the effect of climate change on all these wave characteristics, which may improve the quality of fatigue designs.

The natural variabilities of significant wave height and fatigue damage were evaluated by control simulations. The wind fields and sea states were simulated under the constant external forcing condition. The boundaries of natural variability were defined as 0.95 and 0.05 confidence intervals. It has been shown that all the projected significant wave height and fatigue damage trajectories exceed the lower boundary of natural variability, no matter which time increment is used. It means that human activities (the emission of GHGs) have

Table 5 Comparison of annual fatigue damage in three oil fields

Oil field	Simulations	Time year	Mean 10^{-3}	Std 10^{-3}	CV -	Bias -
Rosebank	Control	1850–1879	8.64	2.1	0.24	-
	RCP85	2011–2020	5.35	1.95	0.36	0.62
		2051–2060	4.61	0.78	0.17	0.53
		2091–2100	3.88	1.12	0.29	0.45
Alma/Galia	Control	1850–1879	1.86	0.73	0.40	-
	RCP85	2011–2020	0.78	0.40	0.51	0.42
		2051–2060	0.81	0.27	0.33	0.43
		2091–2100	0.56	0.21	0.38	0.30
Pierce	Control	1850–1879	2.88	0.99	0.34	-
	RCP85	2011–2020	1.36	0.44	0.33	0.47
		2051–2060	1.40	0.38	0.27	0.49
		2091–2100	1.07	0.27	0.25	0.51

been causing a considerable impact on sea states and structural fatigue damages. In addition, although wave height is the dominant wave characteristic in fatigue calculations, the change of other wave characteristics should also be considered to improve the quality of fatigue designs.

References

Aalberts P, van der Cammen J, Kaminski ML (2010) The Monitas system for the Glas Dowr FPSO. Offshore Technology Conference, Houston

Baede APM, Ahlonsou E, Ding Y, Schimel DS (2001) The climate system : an overview. Cambridge University Press, New York

Bitner-Gregersen EM, Eide L (2010) Climate change and effect on marine structure design. DNVRI Position Pap

Bitner-Gregersen, E.M., Haver, S., 1991. Joint environmental model for reliability calculations

Bitner-Gregersen EM, Horte T, Skjong R, (2011) Potential impact of climate change on tanker design, in: Omae2011: Proceedings of the Asme 30th International Conference on Ocean, Offshore and Arctic Engineering, Vol 2. pp. 805–813. https://doi.org/10.1115/omae2011-50162

Booij N, Ris RC, Holthuijsen LH (1999) A third-generation wave model for coastal regions: 1. Model description and validation. J Geophys Res 104:7649–7666. https://doi.org/10.1029/98JC02622

DNV-GL-AS (2014) Fatigue Assessment of Ship Structures

Dobrynin M, Murawski J, Baehr J, Ilyina T (2015) Detection and attribution of climate change signal in ocean wind waves. J Clim 28: 1578–1591. https://doi.org/10.1175/JCLI-D-13-00664.1

Gómez Lahoz M, Albiach JCC (2005) Wave forecasting at the Spanish coasts. J Atmos Ocean Sci 10:389–405. https://doi.org/10.1080/17417530601127522

Greenhill AG (1886) Wave motion in hydrodynamics. Am J Math 9(1): 62–96

Hanson JL, Phillips OM (2001) Automated analysis of ocean surface directional wave spectra. J Atmos Ocean Technol 18:277–293. https://doi.org/10.1175/1520-0426(2001)018<0277:aaoosd>2.0.co;2

Hasselmann S, Hasselmann K, Allender JH, Barnett TP (1985) Computations and parameterizations of the nonlinear energy transfer in a gravity-wave spectrum. Part II: parameterizations of the nonlinear energy transfer for application in wave models. J Phys Oceanogr 15(11):1378–1391

Hemer MA, Fan Y, Mori N, Semedo A, Wang XL (2013) Projected changes in wave climate from a multi-model ensemble. Nat Clim Chang 3(5):471–476

Janssen PAEM (2008) Progress in ocean wave forecasting. J Comput Phys 227:3572–3594. https://doi.org/10.1016/j.jcp.2007.04.029

Kaminski ML, Aalberts P (2010) Implementation of the Monitas system for FPSOs. Offshore Technology Conference, Houston

Madec, G., Delecluse, P., Imbard, M., Levy, C., 1998. OPA 8 ocean general circulation model reference manual

Morim J, Hemer M, Wang XL, Cartwright N, Trenham C, Semedo A, Young I, Bricheno L, Camus P, Casas-Prat M, Erikson L, Mentaschi L, Mori N, Shimura T, Timmermans B, Aarnes O, Breivik Ø, Behrens A, Dobrynin M, Menendez M, Staneva J, Wehner M, Wolf J, Kamranzad B, Webb A, Stopa J, Andutta F (2019) Robustness and uncertainties in global multivariate wind-wave climate projections. Nat Clim Chang 9(9):711–718

Randall DA, Bony S, Wood RA, Colman R, Fichefet T, Fyfe J, Kattsov V, Pitman A, Shukla J, Srinivasan J, Stouffer RJ, Sumi A, Taylor KE (2007) Climate models and their evaluation, in: climate change 2007: the physical science basis. Contribution of Working Group I to the Fourth Assessment Report of the Intergovernmental Panel on Climate Change. 662

Riahi K, Rao S, Krey V, Cho C, Chirkov V, Fischer G, Kindermann G, Nakicenovic N, Rafaj P (2011) RCP 8.5-a scenario of comparatively high greenhouse gas emissions. Clim. Change 109:33–57. https://doi.org/10.1007/s10584-011-0149-y

Roeckner E, Bauml G, Bonaventura L, Brokopf R, Esch M, Giorgetta M, Hagemann S, Kirchner I, Kornblueh L, Manzini E, Rhodin A, Schlese U, Schulzweida U, Tompkins A (2003) The atmospheric general circulation model ECHAM5. Max Planck Inst Meteorol 349:1–140

Rusu E, Guedes Soares C (2009) Numerical modelling to estimate the spatial distribution of the wave energy in the Portuguese nearshore. Renew Energy 34:1501–1516. https://doi.org/10.1016/j.renene.2008.10.027

Scoccimarro E, Gualdi S, Bellucci A, Sanna A, Fogli PG, Manzini E, Vichi M, Oddo P, Navarra A (2011) Effects of tropical cyclones on ocean heat transport in a high-resolution coupled general circulation model. J Clim 24:4368–4384. https://doi.org/10.1175/2011JCLI4104.1

Shine KP (2010) Radiative forcing and climate change, in: encyclopedia of aerospace engineering. John Wiley & Sons, Ltd. https://doi.org/10.1002/9780470686652.eae526

Sverdrup HU, Munk WH (1952) Wind, sea and swell: the theory of relations for forecasting. Government Print Office, for sale by the Hydrographic Office, Washington, D.C.

Tolman HL (2014) The WAVEWATCH III development group (2014). User manual and system documentation of WAVEWATCH III version 4.18. Tech. Note 316, NOAA/NWS/NCEP/MMAB

Tolman HL, Balasubramaniyan B, Burroughs LD, Chalikov DV, Chao YY, Chen HS, Gerald VM (2002) Development and implementation of wind-generated ocean surface wave models at NCEP. Weather Forecast 17:311–333. https://doi.org/10.1175/1520-0434(2002)017<0311:daiowg>2.0.co;2

Valcke S (2013) The OASIS3 coupler: a European climate modelling community software. Geosci Model Dev 6:373–388. https://doi.org/10.5194/gmd-6-373-2013

van Vuuren DP, Edmonds J, Kainuma M, Riahi K, Thomson A, Hibbard K, Hurtt GC, Kram T, Krey V, Lamarque J-F, Masui T, Meinshausen M, Nakicenovic N, Smith SJ, Rose SK (2011) The representative concentration pathways: an overview. Clim Chang 109:5–31. https://doi.org/10.1007/s10584-011-0148-z

Vanem E, Bitner-Gregersen EM (2012) Stochastic modelling of long-term trends in the wave climate and its potential impact on ship structural loads. Appl Ocean Res 37:235–248. https://doi.org/10.1016/j.apor.2012.05.006

Young IR, Ribal A (2019) Multiplatform evaluation of global trends in wind speed and wave height. Science 364(6440):548–552

Young IR, Zieger S, Babanin AV (2011) Global trends in wind speed and wave height. Science 332(80):451–455. https://doi.org/10.1126/science.1197219

Zou T, Kaminski ML (2016) Applicability of WaveWatch-III wave model to fatigue assessment of offshore floating structures. Ocean Dyn 66:1099–1108. https://doi.org/10.1007/s10236-016-0977-4